# Sediment Grain-Size Composition in the Permafrost Region of the Greater Khingan Range and Its Significance as a Material Source

Lixin Liu [1,2], Shuying Zang [1,2,*], Xiaodong Wu [3], Rui Liu [1,2], Tianrui Li [1,2], Jiaju Zhu [1,2], Li Sun [1,2], Shaoqiang Wu [1,2], Xingfeng Dong [1,2] and Zihao Zhang [1,2]

[1] Heilongjiang Provincial Key Laboratory of Geographic Environment Monitoring and Spatial Information Service in Cold Regions, Harbin Normal University, Harbin 150025, China; lixinliu1999@163.com (L.L.); c4x4yf@stu.hrbnu.edu.cn (R.L.); leetrhlj@163.com (T.L.); 18919096336@163.com (J.Z.); hrbnu_sunli@hrbnu.edu.cn (L.S.); wshaoqiang2023@163.com (S.W.); zhangzihao@stu.hrbnu.edu.cn (Z.Z.)

[2] Collaborative Innovation Center for Ecological Security in Cold Regions of Heilongjiang Province, Harbin 150025, China

[3] Qinghai-Tibet Plateau Cryosphere Observation and Research Station, State Key Laboratory of Cryospheric Science, Northwest Institute of Eco-Environment and Resources, Chinese Academy of Sciences, Lanzhou 730000, China

[*] Correspondence: zsy6311@hrbnu.edu.cn or hsdzsy6311@163.com

**Abstract:** Sediment grain-size distribution (GSD) provides rich information about sedimentary sources and can potentially do the same with regard to environmental and climatic changes. However, neither traditional descriptive statistics nor curving-fitting methods can fully address its complexity. We selected the Greater Khingan Range in northeastern China as the study area and used parameterized end-member analysis (EMA) of the GSD of four drilling cores to extract different end-member (EM) components. The results show that EM1 (mode particle size (Mo): 1.26–1.66 μm) originates from weathering and pedogenesis. The EMs with Mo values of 4.37–5.01 μm represent components transported by the upper westerly wind. EMs with Mo values of 7.58 μm and 11.48 μm represent wet dust deposition and dry dust deposition. The wind transport of particles in winter consists of low-level near-source transport and local-source transport (possibly from the flood plain of the Amur River). Due to the limitations of the EM model, the two sources have one or two EM components: AEM3 + AEM4, BEM3 + BEM4, CEM4, and DEM4. DEM5 is the only large particle-size component and may represent coarse-grained detritus generated via rock weathering. The components related to the winter monsoon and the ^{14}C dating data suggest a weak-strong-weak-strong trend of the winter monsoon since the Marine Isotope Stage 3a (MIS 3a). Our results suggest that the strengthening of the winter monsoons in the previous few thousand years has caused the transportation of coarser grain sizes and further exacerbated permafrost degradation, providing a scientific reference for understanding climate change and the formation and evolution of permafrost in the Greater Khingan Mountains since the MIS 3a.

**Keywords:** permafrost; grain size; end-member; winter monsoon

## 1. Introduction

Permafrost is soil or other materials at or below 0 °C for two or more consecutive years [1]. The Northern Hemisphere permafrost region includes the high-latitude permafrost regions of Eurasia and North America and the alpine permafrost regions of the middle and low latitudes. Approximately 70% of this area is located between 45° N and 67° N [2]. China's permafrost areas are located in northeast China, the western alpine areas, the Qinghai-Tibet Plateau region, and other alpine regions.

The Greater Khingan Range represents the highest-latitude mountains in China and a high-latitude permafrost region. The mountain range was formed during the last glacial

maximum (LGM) [3]. The Greater Khingan Range region is located at the southern margin of the permafrost region in Eurasia. The thermal stability of the frozen soil is low; thus, the area is vulnerable to global climate change. The change in the average temperature trend in China is consistent with that of the global average temperature. However, the temperature rise is higher in northeast China than that observed in the rest of the country [4]. The permafrost in the Greater Khingan Range has shown rapid degradation in recent years, a fact manifested by an increase in the active layer's thickness [5,6] and a northward shift of the southern boundary of the permafrost region [7].

Permafrost degradation is closely related to soil physical properties. Grain-size distribution (GSD) influences the stability, strength, and erosion resistance of soils [8,9]. The composition and properties of rock and soil affect permafrost development through the thermal and physical properties and the water content. The thermal conductivity of hard rock is generally higher than that of the quaternary loose layer. Thus, if all other conditions are equal, the thickness of the frozen soil layer in hard rock is 1.3–1.5 times that of the loose layer [10]. The finer the soil, the stronger its water-holding capacity, making it more suitable for frozen soil preservation [11]. Therefore, coarse soil remains frozen shorter than finer soil. In general, the coarser the particle size and the thicker the active layer, the higher the potential for permafrost degradation. The soil material source is the basis of the GSD and affects the texture of soil; hence, understanding the source of frozen soil is critical for analyzing permafrost degradation.

Previous studies evaluated grain-size parameters and the components' contents to distinguish sediment categories and reveal environmental changes [12–15]. These indicators can only approximate environmental changes but cannot reveal the source of the sedimentary environment; thus, these methods have limitations for use in environmental reconstruction. The extraction of grain-size components sensitive to environmental changes is an important means of analyzing the evolution of a variety of complex environments, such as fluvial lacustrine sedimentary, marine sedimentary, and continental sedimentary environments.

In recent years, the grain-size end-member analysis method has been developed extensively. This rubric assumes that the grain-size distribution of sediments is determined by different provenance or dynamic processes. The essence of this method is to reverse-decompose a certain proportion of different GSDs from the grain-size data of sediments through mathematical algorithms in order to reveal information regarding the provenance and sedimentary dynamics contained in sediments called end members (EMs) [16].

The commonly used methods are divided into two categories, namely, the function-curve-fitting method and the non-parametric decomposition method. The function-curve-fitting method considers that the particle size of sediment carried by a single power follows a certain distribution function in nature. The granularity of sediments of multiple origins can be decomposed into a continuous unimodal distribution through function-fitting operations and parameter settings. The two commonly used function-fitting methods are normal distribution function fitting [17,18] and Weibull function fitting [19,20]. Yu et al. used the Weibull function-fitting method to perform end-member analysis on Hunshandake Sandy to obtain six EMs of eolean sand and indirectly explained the movement direction of eolean sand with different particle sizes [21].

When using the function-curve-fitting method, the number of particle size components and the type of distribution function are set by observing the number and shape of the peak of the particle size frequency distribution curve, which may be affected by sample contingency and researcher subjectivity [16,22]. The non-parametric decomposition method is used to extract the information from the size distribution data in batch samples based on feature space analysis and decompose the size distribution into the proportional contribution of an optimal sequence [23]. Combined with the existing geological records, Wang et al. used a non-parametric end-member analysis model to divide the sediments from the west coast of Bohai Bay into six EMs and used their end-member content and

other features to make speculations about the sea-level alterations and climate change in this region in history [24].

Weltje (1997) put forward the particle size element model algorithm (end-member modelling algorithm, EMMA). This is a non-parametric decomposition method that is based on determining the correspondence between principal component analysis, factor rotation, and the negative least-squares method decomposition size data dynamics. Grain-size end-member shape, position, and parameters depend on the dataset itself. Requiring no artificial setup, these factors can be used to synchronously extract information from a large quantity of sediment particle size data in a certain area or at a certain depth [16]. However, when using this method to decompose samples with a high mixing degree, some components may span the whole grain size, which does not indicate specific deposition dynamics. There may also be problems with the presence of multiple peaks at the coarse-grain end or the omission of interpretation at the fine-grain end [19,25].

In order to solve the problem, Paterson and Heslop (2015) proposed a parameterized EMA method [22] that could combine the advantages of the above two methods. Subsequently, it has been widely used in this area of study. Zhao et al. analyzed grain size using the parametric EMA method (Gen.Weibull: General Weibull.) and investigated the loess of Shengshan Island in the East China Sea since LGM primarily came from three sources, namely, the far-source component of upper westerly wind, the component of floating dust transported over a long distance as the wind weakened, and the component of near-surface transport by winter wind [26]. At the same time, Chen et al. also used this EMA method to obtain loess provenance information of the Miaodao Islands since the late Pleistocene, and the wavelet analysis proved that the summer monsoon showed cyclicities of 0.6 ka, 1.4 ka, 2.2 ka, and 5.7 ka and that the winter monsoon showed cyclicities of 0.6 ka, 1.6 ka, 2.6 ka, 3.6 ka, and 5.5 ka [27]. The method can also be applied to lake sediments. Fang et al. used the parametric EMA method to analyze lake sediments in the Wuwei region of China and obtained three EMs: The EM1 contains a clay component moved by high-altitude wind and a silt component moved by regional wind. The EM2 may be related to sediment transportation into the lake via surface runoff. The EM3 may represent coarse-grained saltation deposited by flooding or the lake after secondary perturbation [28].

However, few studies have assessed the sedimentary sources in permafrost regions. This study focuses on permafrost sediments in the Greater Khingan Mountains and uses parameterized EMA to extract sensitive components in order to analyze the source of sediment material. The results provide new insights into the sources of permafrost and its evolution.

## 2. Regional Overview

The study area is located in the northernmost part of China on the Northern Slope of the Great Khingan Range (Figure 1). Tectonically, the area belongs to the Erguna block in the eastern section of the Xingmeng Orogenic Belt [29]. Due to tectonic faults, fault basins formed in the area and the typical landforms are low hills and valleys. The area has a cold temperate continental monsoon climate, with short, rainy summers and long, cold winters. The average annual temperature is −3.9 °C, the average temperature in January is −29.7 °C, and the average temperature in July is 18.4 °C. The average annual precipitation is about 450 mm/a, and the average frost-free period is 86.2 d. The Heilongjiang (Amur) River and several small tributaries flow through the northern part of this region. Common forest types in the Greater Khingan Range are coniferous forests dominated by *Larix gmelinii* and broad-leaved forests dominated by *Betula platyphylla* [30,31]. Mohe City in the Greater Khingan Range is located on the south bank of the upper reaches of the Amur River, which is the boundary between China and Russia. The Huzhong District is located at the north foot of the Illehuli Range within the Greater Khingan Range. The terrain is high in the west and low in the east. Temperatures remain around −40 °C for about one month, and the lowest recorded temperature is −53.2 °C [32]. The area has the largest distribution of *L. gmelinii* in the cold temperate zone [33].
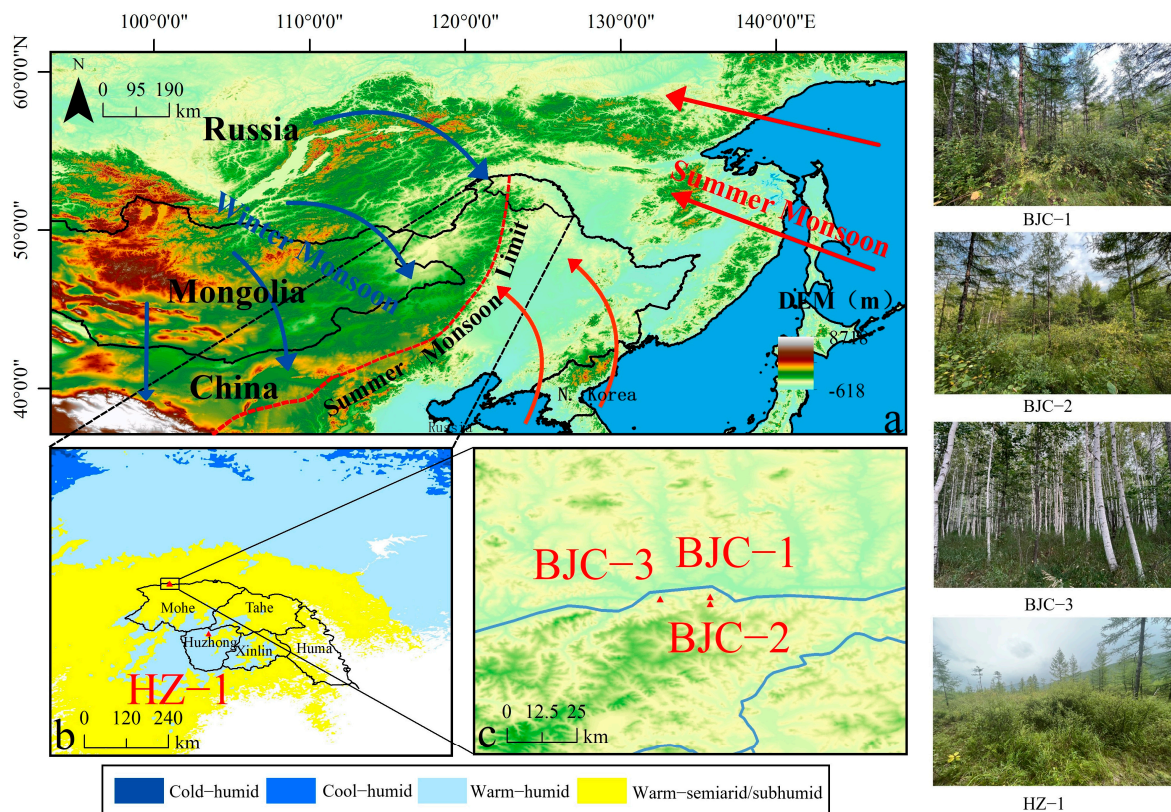
**Figure 1.** Overview of the study area: (**a**) location of the study area, (**b**) type of permafrost and sampling sites [34], and (**c**) sampling sites in the Beiji Village. (BJC-1, BJC-2, and HZ-1 were collected from *L. gmelinii* forest, and BJC-3 was collected from *B. platyphylla* forest).

## 3. Materials and Methods

### 3.1. Lithology and Chronology

We obtained four soil cores in the northern part of the Greater Khingan Range and described the lithology at the site based on the color and sedimentary characteristics of the cores (Figure 2). The core is divided into active, frozen, and non-frozen layers based on the frozen state of the core, and samples are taken based on the active layer (10 cm), frozen layer (20 cm), and non-frozen layer (20 cm) for grain-size tests. The cores (BJC-1 (755 cm), BJC-2 (665 cm), BJC-3 (742 cm), and the Huzhong District core HZ-1 (844 cm)) are denoted as A, B, C, and D, respectively, in this study. The surface vegetation of the BJC-1 and BJC-2 sampling sites in Beiji Village consists of *L. gmelinii* forest (302 m above sea level) and that of BJC-3 is *B. platyphylla* forest (326 m above sea level). The HZ-1 surface vegetation in Huzhong predominantly comprises *Carex meyeriana Kunth* (657 m).

Twelve soil samples from the BJC-3 core (705 cm, 535 cm, 435 cm, 195 cm, 105 cm, and 15 cm) in Beiji Village and the BJC-2 core (640 cm, 453 cm, 380 cm, 193 cm, 115 cm, 105 cm, and 10 cm) were sent to the BETA Laboratory in Miami for radiocarbon ^{14}C dating. The test data were calibrated using the INCAL20 database [35] and the Calib 8.2 software [36], and a complete core dating framework was established using the Bacon age-depth model [37] in R (Figure 3).
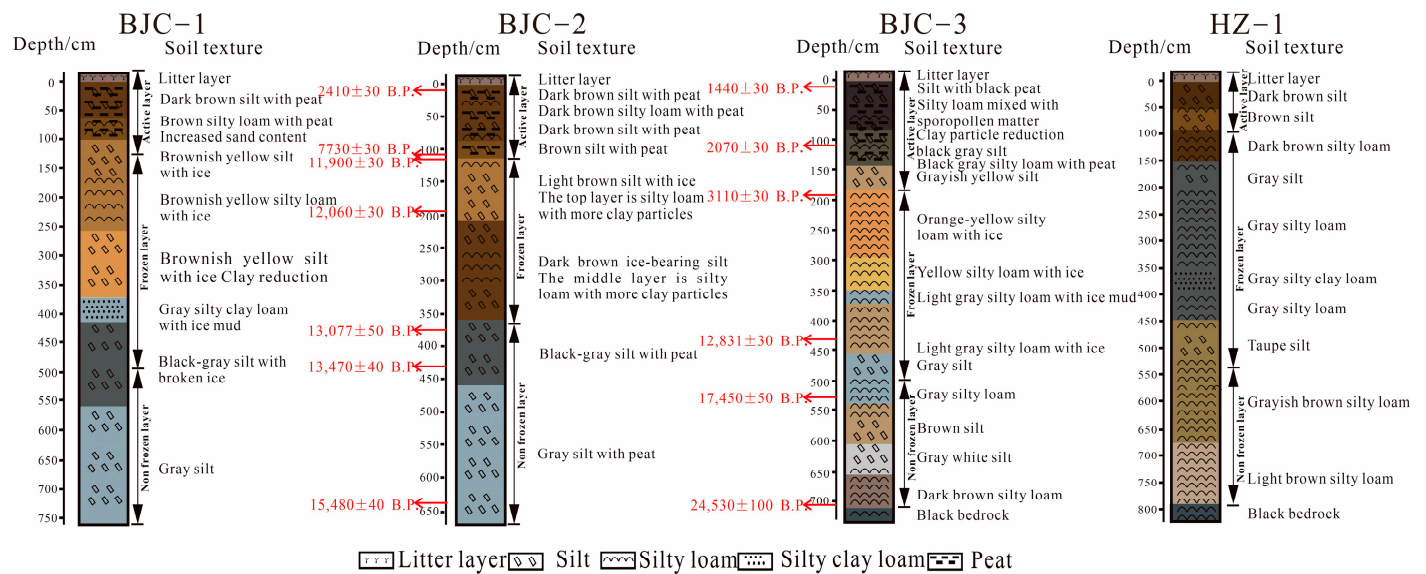
**Figure 2.** Description of the soil texture of the cores and AMS radiocarbon dating sampling depth.
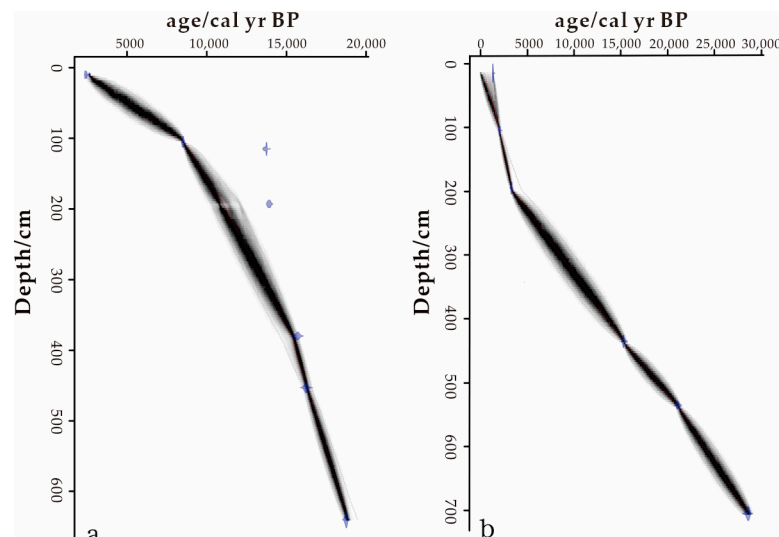
**Figure 3.** Bacon age-depth model. (**a**) age of BJC-2. (**b**) age of BJC-3.

### 3.2. Grain-Size Analysis

The grain size of the samples was measured using a laser particle analyzer Malvern Mastersizer 2000 (Malvern Panalytical Ltd., Malvern, UK). The grain-size distribution was calculated for 45 grain-size classes within a measuring range of 0.01~2000 μm. The sample preparation for the grain-size analysis included the wet oxidation of organic matter by adding 10 mL of 30% $H_2O_2$ per 1.5 g dry sample. Carbonates were dissolved after being boiled with 10 mL (10% hydrochloric acid) for 10 min. The glass beakers were filled with 150 mL of distilled water, and the suspended particles were left to deposit. After siphoning the supernatant water, 10 mL of 0.05 mol/L $(NaPO_3)_6$ was added, and the residue was dispersed for 5 min in an ultrasonic bath before the measurement was conducted. The pump speed of the laser particle size analyzer was fixed at 2200 rpm. The final result was an average of five measurements.

The particle size parameters were calculated by the moment method [38]. The software package "AnalySize", developed using the Matlab programming language, was adopted to implement the parametric EMM method [39,40]. The Weibull function is commonly referred to as the two-parametric Weibull distribution, whereas the Gen. Weibull function

is referred to as the three-parametric Weibull distribution. Both functions can be used for single-sample unmixing (SSU) and in EMM methods [41]. For SSU, it is difficult to separate similar end members. However, EMMA has a better capability to distinguish these end members because all samples are used in computations. Due to the limitations of the EMMA mathematical model (all samples share one group of end members), the variations in end-member distributions will be coupled with variations in end-member abundances. If the variations in distributions are extremely important for a certain dataset, SSU will yield a better solution than EMMA [41].

The component structures of the GSDs, unmixed by the SSU method, contain abundant and valuable sedimentological and paleoenvironmental information that can be revealed via statistical analysis [42]. The results of SSU provide process-related information about individual GSDs and the associated between-sample variability, while the results of EMM represent general states of the distributions of grain assemblages averaged at a specified spatio-temporal coordinate [41,42]. The EMMA method can better separate the mixed-end EMs from the whole sample in order to obtain accurate source information. In 2015, Paterson et al. proposed a parametric method based on the Weibull distribution to conduct EM analysis of grain-size data (Gen. Weibull) using non-negative matrix factorization (NMF) [22]. This method compensates for the deficiencies of the grain-size components selected via Weibull fitting to determine deposition dynamics and transport modes and provide descriptive statistics for and describe the physical significance of the particle-size EMs [43]. If the EM frequency distribution curve has multiple peaks after EM decomposition, it is difficult to explain the dynamic components represented by the EMs because the particle size of different sediment sources is not known due to sorting during transport. Under ideal conditions, i.e., a relatively stable transport medium and dynamic action, the GSD curve of sediments has a single peak. However, in reality, sediments come from different sources and have different transport modes. Thus, the particle size distribution curve has multiple peaks [44]. This curve can be inverted using parametric EM analysis in order to quantify the contribution of various transport media and dynamics during deposition. Generally, the particle size distribution curves derived from non-parametric EM analysis have multiple peaks, whereas those obtained from parametric methods have single peaks. Therefore, we selected the Gen. Weibull method for performing the EM analysis of the samples.

### 3.3. Elemental Analysis

In this experiment, 0.1 g samples were digested via the $HCL\text{-}NHO_3\text{-}HF\text{-}H_2O_2$ digestion method (Anton Paraton-AAR). After digestion, they were put into a heating tank for acid removal. Finally, the volume was set to 50 mL and the samples were put into the sample bottle. The Agilent 7500c (Agilent Technologies, SAN jose, California) inductively coupled plasma mass spectrometer was used to perform elemental analysis, and the standard soil for soil composition analysis was used for comparison. The standard curve of the calibration solution was determined by the American Agilent standard solution, and the standard error of the quality control sample was not more than 5%.

## 4. Results

### 4.1. AMS Radiocarbon Dating Results

Radiocarbon dating showed a difference in the deposition between the *L. gmelinii* forest "BJC-2" and the *B. platyphylla* forest "BJC-3" (Table 1). After 5 ka BP, the deposition rate of the larch forest decreased, while that of the birch forest increased. The $^{14}C$ age at the bottom of hole B is 15.48 ka BP, which is from the last deglacial period. The $^{14}C$ age at the bottom of hole C is 24.53 ka BP, which is the peak of the LGM (26.5–19.0 ka BP) and represents the coldest period in China since the last ice age. Eastern China was affected by the winter monsoon, and the climate was cold and dry, i.e., conducive to permafrost development [45,46].

**Table 1.** Results of radiocarbon dating.

| Core | Depth/cm | Frozen State | AMS $^{14}$C /a B.P. | Error± /a B.P. | Median Calendar Age/cal.a.BP./2σ | 2σ-Corrected Calendar Age Range/cal.a.BP |
|---|---|---|---|---|---|---|
| BJC-2 | 10 | Active layer | 2410 | 30 | 2433 | 2349~2497 |
| | 105 | Active layer | 7730 | 30 | 8499 | 8424~8554 |
| | 115 | Active layer | 11,900 | 30 | 13,765 | 13,606~13,717 |
| | 193 | Frozen layer | 12,060 | 30 | 13,917 | 13,808~13,960 |
| | 380 | Non-frozen layer | 13,077 | 50 | 15,676 | 15,493~15,852 |
| | 453 | Non-frozen layer | 13,470 | 40 | 16,236 | 16,064~16,371 |
| | 640 | Non-frozen layer | 15,480 | 40 | 18,793 | 18,710~18,860 |
| BJC-3 | 15 | Active layer | 1440 | 30 | 1331 | 1297~1373 |
| | 105 | Active layer | 2070 | 30 | 2031 | 1973~2117 |
| | 195 | Active layer | 3110 | 30 | 3328 | 3234~3391 |
| | 435 | Frozen layer | 12,831 | 30 | 15,315 | 15,186~15,506 |
| | 535 | Non-frozen layer | 17,450 | 50 | 21,031 | 20,885~21,295 |
| | 705 | Non-frozen layer | 24,530 | 100 | 28,778 | 28,642~28,966 |

*4.2. Composition of Sediment Grain Size*

Shepard's sediment classification diagram was used to assess the data of grain-size components measured during the experiment (Figure 4). The dominant soil texture in the Greater Khingan Range is that of clayey silt, whereas the soil texture of the cores obtained from the *L. gmelinii* forest area (A, B, and D) is coarse. Silty sand, sandy silt, clay silt, silty clay, and sand silty clay are common texture types. Only silty clay and clay sand occur in the core obtained from the *B. platyphylla* forest area (C). In summary, clayey silt is the dominant soil texture in the cores obtained from Huzhong and Beiji Village. The sediments differ slightly for different types of vegetation areas, i.e., birch forests have finer soils than larch forests.
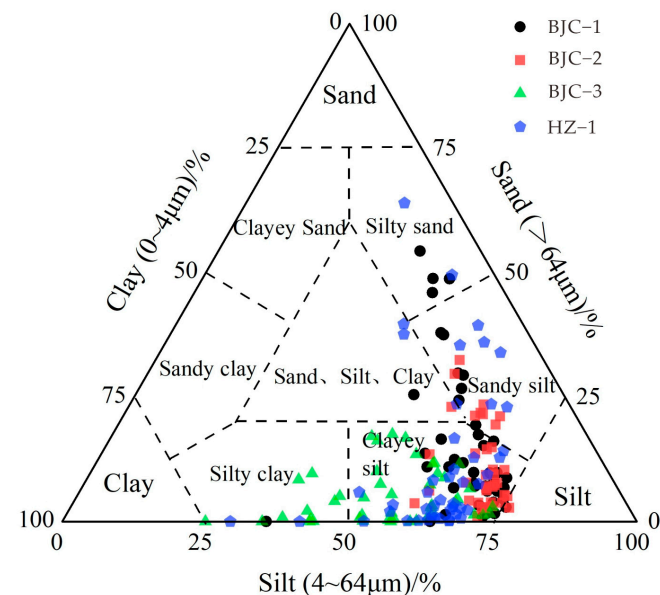
**Figure 4.** Shepard's sediment classification diagram.

*4.3. Results of End-Member Modeling Analysis*

Three indicators are typically used to assess the number of EMs: the $R^2$ value (linear correlations: these indicate the pertinence between the original granular data and the metadata at the fitting end), the EM $R^2$ value (end-member correlations: a large value indicates overfitting), and θ (angular deviation: the end-member metadata and the GSD

are distributed at different angles). Because the number of end members should not be too high (this causes excessive separation, increasing the complexity of the analysis) or too low (it is difficult to separate the source and power), this paper selects the end members from 3 to 5 (Figure 5). The larger the $R^2$ and the smaller the EM $R^2$ and θ, the better the results. Three to five EMs were selected for the different cores. For core A, the EM $R^2$ (0.044) was the smallest, and θ < 5°; thus, four EMs were selected. Four end elements were selected for core B (EM $R^2$ = 0.081 and θ = 2.954°) and core C (EM $R^2$ = 0.271 and θ = 3.953°). Five EMs were chosen for core D. The EMs of the four cores were called AEM, BEM, CEM, and DEM.
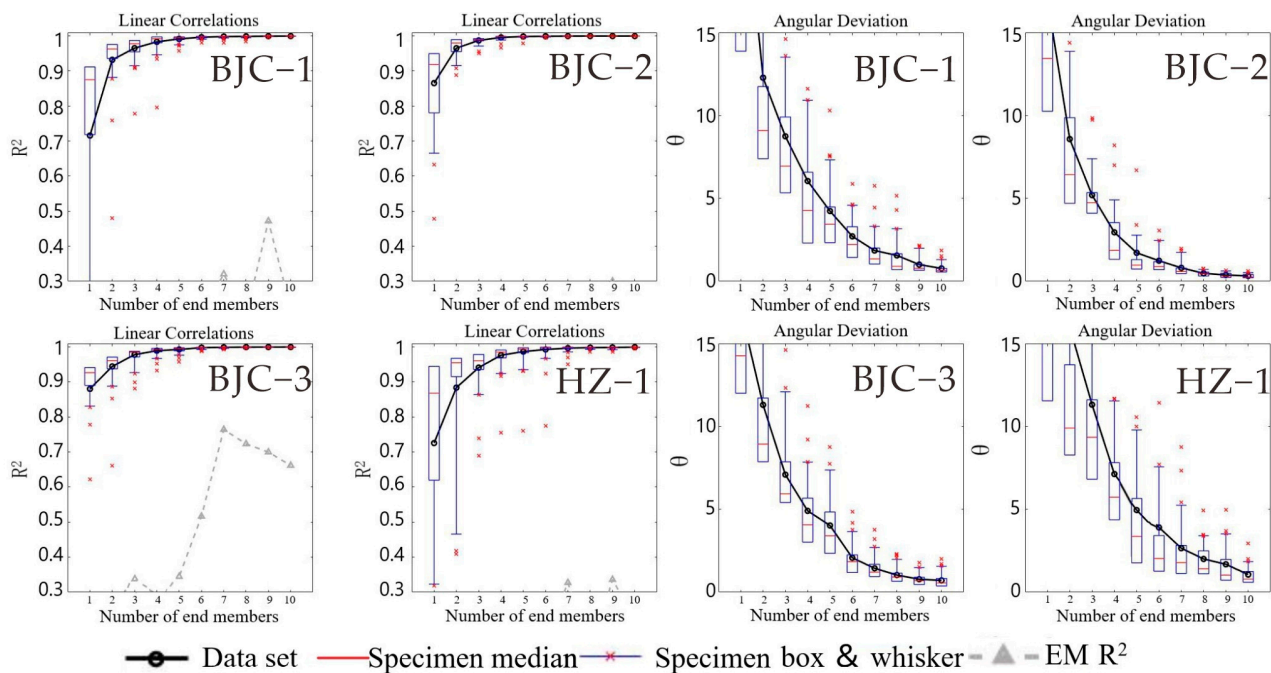
**Figure 5.** End-member evaluation results.

The EM modeling results are shown in Figure 6 and Table 2. The Mo values of A are 1.66 μm, 7.58 μm, 22.91 μm, and 104.71 μm; those of B are 1.26 μm, 7.58 μm, 26.30 μm, and 79.43 μm; those of C are 1.45 μm, 4.37 μm, 7.58 μm, and 79.43 μm; and those of D are 1.66 μm, 5.01 μm, 11.48 μm, 45.70 μm, and 831.76 μm. The standard deviation of the EMs of A is 1.83–2.40, with an average of 2.07, and that of B is similar (2.03–2.43), with an average of 2.17. The standard deviation of CEM4 is 6.81, the sorting is very poor, and the particles are dispersed. Sk (Coefficient of Skew) = −0.05, showing a weak negative bias, and the $\sigma_i$ (standard deviation) of the EMs of D is 1.74–2.91, with an average of 2.15.

**Table 2.** Standard deviation of the end members of the cores.

| Core | EM1 | EM2 | EM3 | EM4 | EM5 |
|------|-----|-----|-----|-----|-----|
| BJC-1 | 2.40 | 1.83 | 2.04 | 1.99 | - |
| BJC-2 | 2.43 | 2.11 | 2.03 | 2.12 | - |
| BJC-3 | 2.24 | 1.69 | 1.88 | 6.81 | - |
| HZ-1 | 2.08 | 1.74 | 2.13 | 2.91 | 1.89 |

EM5 only occurred in the active layer of core D. The EM contents of CEM 4, AEM 3 + AEM 4, BEM 3 + BEM 4, and DEM3 + DEM4 were all about 50%, whereas the EM composition of A and B showed similar changes with the depth (Figure 7). This illustrates that some of the end members extracted via the EMA method are not completely separated.
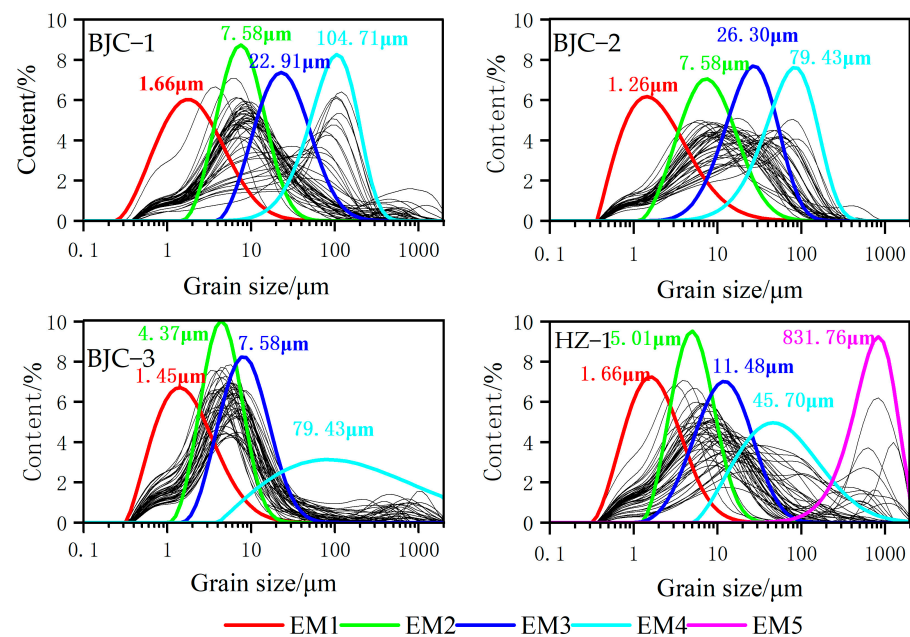
**Figure 6.** End-member modeling results (color curve) and grain-size distribution (black curve).
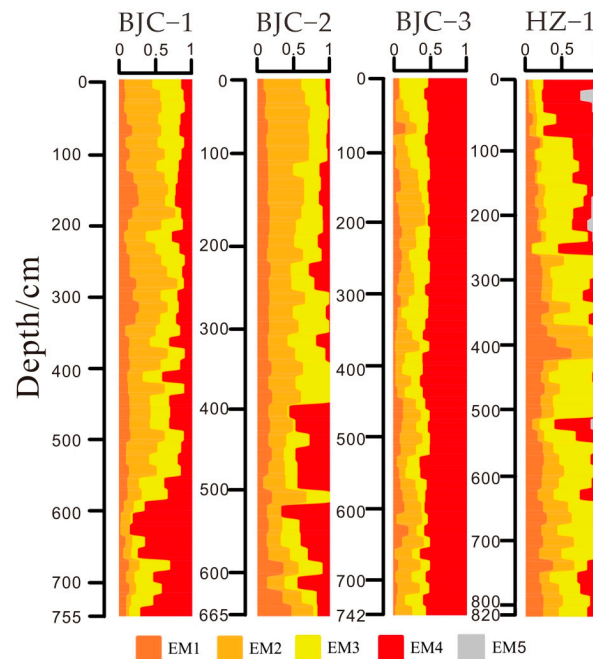
**Figure 7.** The end-member values of the cores at different depths.

*4.4. Elemental Determination Results*

The vertical distribution of Al and Fe content obtained by the experiment is shown in Figure 8, in which the average Al content of each core is 8.23 g/kg (BJC-1), 6.23 g/kg (BJC-2), 13.1 g/kg (BJC-3), and 16.1 g/kg (HZ-1), and the average Fe content is 25.36 g/kg (BJC-1), 28.44 g/kg (BJC-2), 39.90 g/kg (BJC-3), and 28.37 g/kg (HZ-1). The Al content of *B. platyphylla* dominated by vegetation (BJC-3) and *C. Kunth* dominated by vegetation (HZ-1) is significantly higher than that of *L. gmelinii*, and the Fe content of BJC-3 core is the highest.
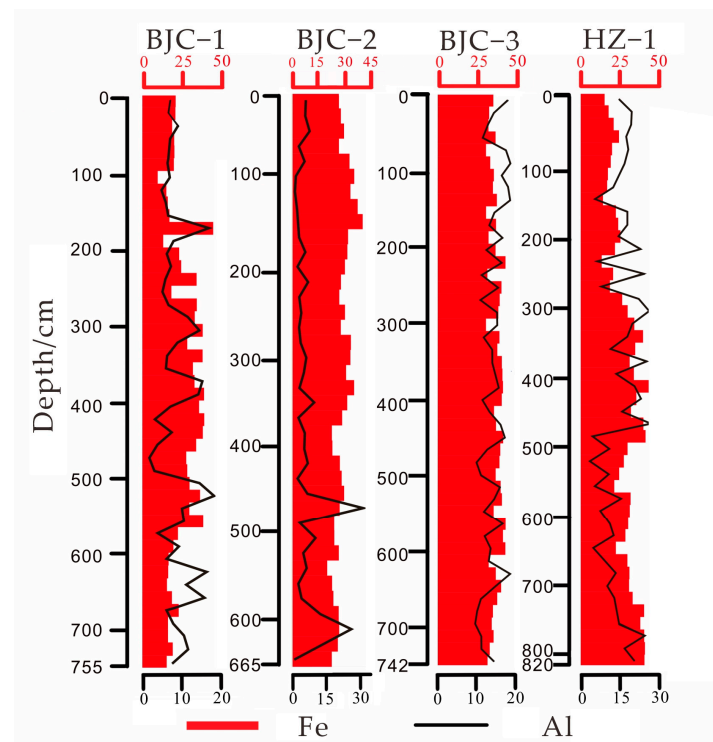
**Figure 8.** The variation curve of Fe and Al content in each core with depth.

## 5. Discussion

### 5.1. Sediment Source Assessment Using Grain-Size End Members

At present, there are two views on ultrafine fractions. The first view is that fine particles are transported or adhere to the surface of coarse particles in the form of aggregates [47], and the other is that their formation is related to pedogenesis [48]. The correlation analysis of the four core's EM components shows no positive correlation between EM1 and Md (median diameter, r: 0.248~0.800) and Mz (median size, r: 0.262~0.550). The coarser the particles, the greater the values of Md and Mz, indicating that the fine particles in this paper are not the materials that adhere to the coarse particles. Therefore, the adhesion or aggregation hypothesis may not explain the transport type of EM1. The geochemical properties of Al show that the content of Al is positively correlated with weathering intensity; the vegetation grows vigorously on the wet surface; the roots absorb $Fe^{3+}$ and $Al^{3+}$ ions more strongly [49]. So the Fe + Al content can indicate the strength of weathering into the soil. In this study, the EM1 component was positively correlated with Fe + Al content (r: 0.092~0.479) (Figure 9). The EM1 component of the four cores is primarily clay, accounting for 70.51–85.90%. It is the EM component with the largest clay content. The Mo is in the range of 1.26–1.66 μm. It is generally believed that the clay component with a particle size of less than 2 μm is related to weathering and reflects shifts in the water table [48]. Thus, EM1 may represent weathering or the pedogenic component.

The EM2 component Mo values of A and B are 7.58 μm and those of C and D are 4.37 μm and 5.01 μm, respectively. It is widely believed that soils with a particle size in the range of 2–10 μm are rarely affected by weathering [50]. When micron-sized particles are transported by the wind, they do not settle readily due to their low weight. The prevailing northwesterly and westerly winds in the study area are within the influence range of the westerly belt. Particles <20 μm are dispersed over a large area and transported over hundreds or thousands of kilometers at high altitudes [51]. These particles typically travel from high altitudes to downwind regions [47]. The size of particles transported at high altitudes on the Loess Plateau ranges from 2 μm to 8 μm [50]. EM unmixing for several profiles in the northern Qilian Range showed that particles with sizes of 6 μm to 20 μm were transported at high altitudes over long-distance suspension [52]. The Mo values of

CEM3 and DEM3 in this study were 7.59 μm and 11.18 μm, respectively, indicating that they were wind-transported. It is generally believed that a single peak in the GSD curve represents a single driving force or source of particle deposition, and the sharper the peak, the more likely it will be that there is a single source [19,20,44]. The comparison of the GSD curves for AEM2, BEM2, CEM2, DEM2, CEM3, and DEM3 and for windblown sediment in different regions is shown in Figure 10 to allow readers to access the source components.
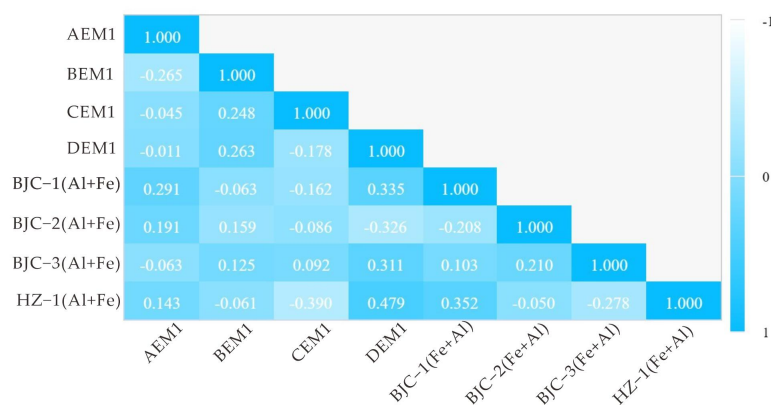
**Figure 9.** Pearson correlation between EM1 and Fe + Al.

We found that CEM2, DEM2, Xifeng laterite, and Xi 'an loess have similar Mo values, indicating that CEM2 and DEM2 were likely transported at high altitudes by the westerly wind. AEM2, BEM2, CEM3, typical Harbin loess [54], and modern spring mud rain in Nanjing [56] have similar Mo values and GSD curves, suggesting that the sedimentation of AEM2, BEM2, and CEM3 was accompanied by precipitation, resulting in wet deposition. We define these qualities as the strength of the East Asian summer monsoon.

The sedimentary characteristics of the "rain dust" indicated that it originated from distant fine dust produced by northern dust devils. The southward movement of a cold front provides the energy for the wind transport of the dust, and the removal of fine dust by the warm and wet air in the lower reaches of the Yangtze River promotes the occurrence of wet dust. At the same time, under the background of large-scale dust activities in the north and the southward invasion of cold waves, the distant dust can also be transported to the lower reaches of the Yangtze River in the form of "dry dust", and DEM3 is similar to the dry dust deposited in Harbin. Thus, it is inferred that DEM3 may be a component of dry dust deposition.

The source of the particle composition can be analyzed using time-series climatic data. The dating data of cores B and C and the BEM2 and CEM3 with Mo = 7.58 μm were compared with the temperature and humidity changes in Baiyangdian and Ningjinbo in the last 32 cal kyr BP years to clarify the composition of the EM components. Similar changes were found elsewhere (Figure 11). The temperature and precipitation in the Asian monsoon region during the East Asian Summer monsoon changed synchronously over the past 30,000 years [57]. The BEM2 and CEM3 values were lower in the cold and dry climate of the LGM, whereas the BEM2 and CEM3 values increased during the Holocene warm period, which was similar to the trend of temperature and precipitation in East Asia. Along these lines, combined with the GSD of the end-member frequency, it is considered that the dust fraction precipitates with precipitation under the East Asian Summer monsoon. Although A and D lacked age data, AEM2, BEM2, and CEM3 showed similar trends. In contrast, DEM3 exhibited the opposite trend, i.e., the closer a component was to the surface, the lower its content, indicating that the component can indicate the degree of drought in the region. Combined with the EM frequency distribution curve, this result suggests a dry dust deposition similar to that in Harbin. In summary, we believe that DEM3 is associated with dust storm sedimentation in dry weather (dry dust).
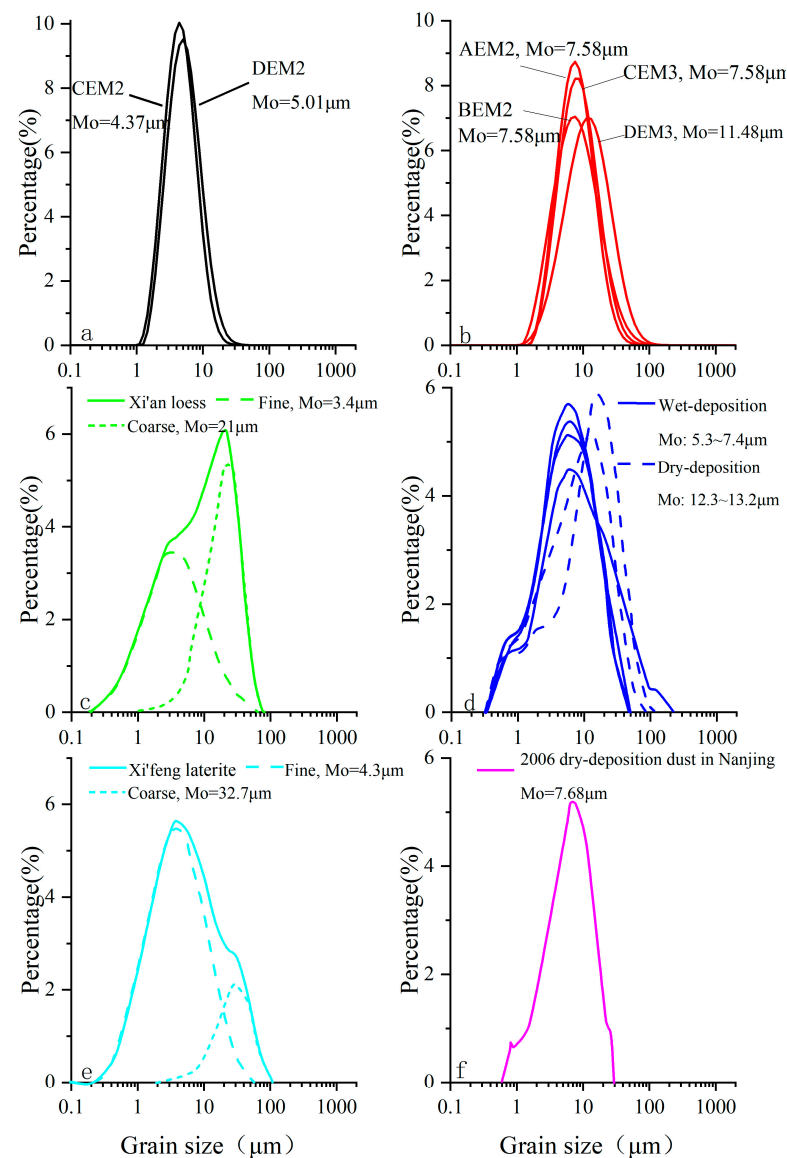
**Figure 10.** Comparison of grain-size distribution curves derived from this study and for windblown sediment in different regions. (**a**) CEM2 and DEM2 components; (**b**) AEM2, BEM2, CEM3, and DEM3 components; (**c**) Xi 'an loess based on end-member modeling: the Mo of the fine particles is 3.4 μm (quaternary upper northwest wind), and that of the coarse particles is 21 μm [53]; (**d**) Mo of wet dust is 5.3–7.4 μm and Mo of dry dust is 12.3–13.2 μm during a sandstorm in Harbin [54]; (**e**) Xifeng laterite: the Mo values of the fine and coarse particles are 4.3 μm and 32.7 μm, respectively [55]; (**f**) 2006 Nanjing rain dust, with Mo 7.68 μm [56].

The dust dynamics model shows that dust particles with a size >20 μm were transported at low altitudes (below 100 m) under normal conditions, and that the transport altitude did not exceed 1 km under strong storm conditions. The EM component with a size >20 μm in this study was calculated as follows [58]:

$$Y = -3.5688 \times Mz + 3.7016 \times Sd2 - 2.0766 \times Sk + 3.1135 \times Kg \tag{1}$$
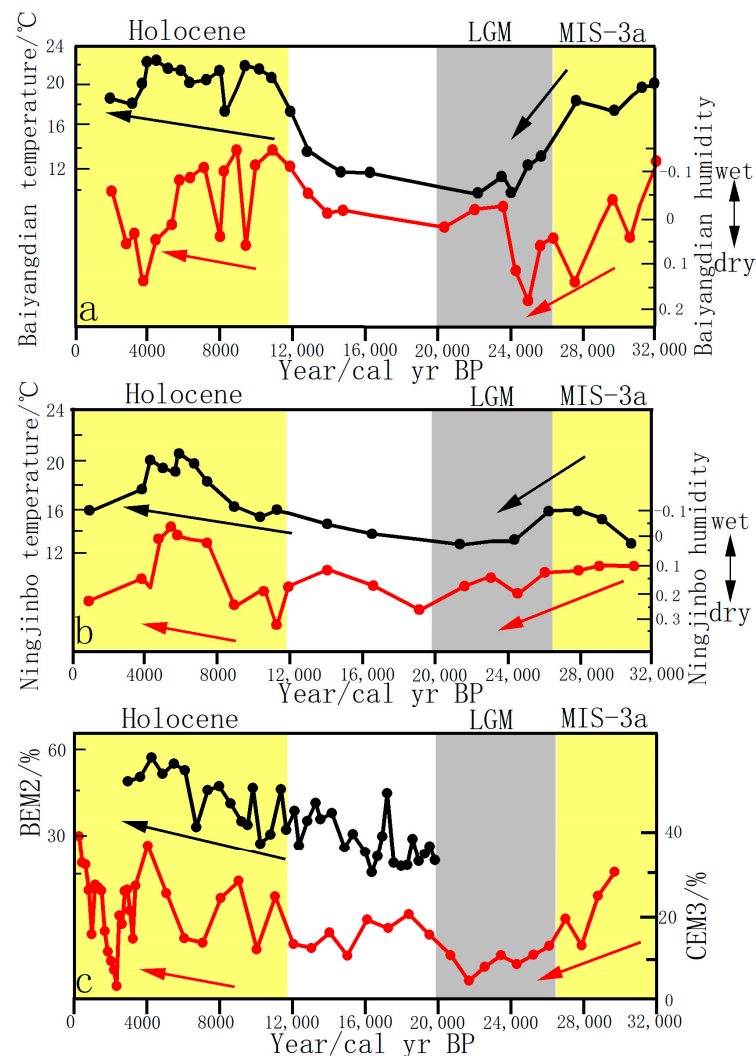
**Figure 11.** Changes in temperature and humidity at Baiyangdian Lake (**a**) and Ningjinbo Lake (**b**) and the BEM2 and CEM3 components (**c**) (Reference data from [57]).

All of the calculated Y values < −2.7411 were considered aeolian sediments that were transported by strong winds. Medium-to-coarse silt and fine sand particles with sizes of 20–70 μm can be suspended in dust devils, and the transport distance in the atmosphere is only a few hundred meters. Additionally, particles larger than 30 μm can migrate at most 30 km from the source area in strong storms [47,59]. Under extreme storm conditions, they can be suspended near the surface and transported 500–1500 km from the source [60]. Wang et al. [61] extracted the EM components for a particle size range of 8.14 μm to 493.63 μm and obtained a Mo of 121.8 μm. The authors stated that the fine particles of this component could be transported a long distance during a strong East Asian winter monsoon, whereas coarse particles were transported and deposited nearby during the winter monsoon. The EM3 (Mo: 25–28 μm) + EM4 (Mo: 44–45 μm) components of Xiashu loess extracted using the EMA were considered to be different components of low-altitude near-source + local-source transport by strong winter winds [21]. Sun et al. conducted a study of particle sizes on the Loess Plateau and found that the coarse EM component (21–54 μm) is mainly transported at a low altitude and short distance [53]. They believed that the transport distance was short, and that transport occurred at low altitudes. Prins and Vriend analyzed multiple soil profiles in the Loess Plateau [62]. The coarse-grain component was divided into two EMs: One had a grain size of 40 μm (DEM4), was likely going to be transported a short distance, and reflected a change in the winter

wind; the other component's size was slightly larger than 60 μm (AEM4, BEM4, and CEM4). It might have been transported a short distance by saltation and also reflected a change in the winter monsoon. The sediments of Tolbo Lake were controlled by the Siberian High, and the components with a median particle size of 15–84 μm and larger than 84 μm are good indicators of regional dust storms and local sandstorms, respectively [63]. Vandenberghe [64] believed that dust particles with sizes of 25 to 65 μm (e.g., AEM3, BEM3, and DEM4 components in this paper) had similar transport patterns, but that the wind intensity, local topography, and surface conditions resulted in differences in the particle size distribution. Sun et al. used the Weibull function to extract coarse particles (40–50 μm) from a loess sequence in the northern part of the Loess Plateau [53]. It was inferred that the coarse-grained components were intermittently suspended and transported near the surface when dust devils advanced or retreated due to the regional winter wind. Dietze et al. used an EM model to extract the 125 μm-particle-size component from data collected at East Jicona Lake in the northeastern part of the Tibetan Plateau. The winter winds blew nearby coarse dust to this location, and this component represents the transport characteristics and evolution of winter winds [20]. Li et al. observed that the EM components with a Mo of 63 μm were significantly affected by the Tibetan plateau winter wind. Sand particles with a size greater than 63 μm were only transported near the surface for short distances by saltation and rolling due to their large particle size [65]. Grains with a particle size greater than 63 μm transport distance depended on the grain size in the source area, the slope of the sedimentary surface, the wind energy, and other factors and generally occurred at different heights above the floodplain [50]. In contrast, those with a particle size greater than 75 μm came from nearby source areas, such as the river terrace, sandy bottom of outcrops, or dry riverbeds, and the transport distance was short, i.e., within a few hundred meters or several kilometers [64].

Our cores A, B, and C were obtained close to the Amur River basin, and all had EM components: AEM4 (Mo = 104.71 μm) and BEM4 (Mo = 79.43 μm). In summary, these were local-source components transported over short distances by strong winter wind erosion and very likely comprised sandy material from the flood plain of the Amur River. AEM3 (Mo = 22.91 μm) and BEM3 (Mo = 26.30 μm) were intermittently suspended and transported near the surface by winter winds. However, CEM4 (Mo = 79.43 μm, $\sigma_i$ (standard deviation) = 6.81) and DEM4 (Mo = 45.70 μm, $\sigma_i$ = 2.91) had poorly sorted particle sizes. In this particle size range, loess sediments affected by fluvial processes (the fluvio-aeolian loessic) typically have a Mo of 35–55 μm based on global studies [66,67]. They are generally poorly sorted and have a low bias, and most consist of clay and fine silt (hydrostatic sedimentation) or coarse silt and sand (river transport) [64]. However, CEM4 (Mo = 79.43 μm, $\sigma_i$ = 6.81) and DEM4 (Mo = 45.70 μm, $\sigma_i$ = 2.91) did not contain clay and had positive skewness Sk (CEM4: 0.16) or polar positive skewness Sk (DEM4: 0.36). Along with the EM results of A and B, these findings indicate that these EM components may have a mixed nature. This renders them inseparable via the EMA method and suggests that they represent low-altitude near-source and local-source components transported by the prevailing winter monsoon.

The Mo of DEM5 (831.76 μm) indicated the presence of coarse sand with a large particle size, which was mainly distributed in shallow soil (Figure 7). Hard rocks and minerals close to the surface undergo physical and chemical changes due to contact with the atmosphere, water, and organisms. However, biochemical weathering is relatively weak during permafrost development, whereas petrophysical weathering is strong. Seasonal freeze-thaw processes form stone rings, stone rivers, and similar structures. Coarse-grained soil is usually proto-rock debris formed by the physical weathering of rocks. The coarse-grained detrital minerals larger than 500 μm are generally quartz [68]. They are relatively stable and exhibit slow physical and chemical weathering. Performing mechanical grinding and abrasion experiments on different soft and hard rocks and minerals (carbonate and silicate minerals, quartz) has indicated that the fragmentation of rocks and minerals causes a special fragmentation "fine gravel-coarse sand" peak (the scope is −4–1 Φ; 32–0.5 mm) [69].

Therefore, the DEM5 component is very likely material produced by the weathering of surface rocks.

The source attributes of the EM components are listed in Table 3. The regional source compositions are complex and diverse; therefore, the EM components extracted via the EM analysis method represent the dominant sources. However, the sediment particle sizes contributed by the same source (the EM components) are consistent. The difference in dominant sources leads to the different soil textures.

**Table 3.** Mode particle sizes and sources of different end members.

| Core | EM1 | EM2 | EM3 | EM4 | EM5 |
|------|-----|-----|-----|-----|-----|
| A | 1.66 μm Weathering and pedogenesis | 7.58 μm The strength of the East Asia summer monsoon (wet dust) | 22.91 μm Low-altitude near source | 104.71 μm Local source | - |
| B | 1.26 μm Weathering and pedogenesis | 7.58 μm The strength of the East Asia summer monsoon (wet dust) | 26.30 μm Low-altitude near source | 79.43 μm Local source | - |
| C | 1.45 μm Weathering and pedogenesis | 4.37 μm Upper westerly transport | 7.58 μm The strength of the East Asia summer monsoon (wet dust) | 79.43 μm Low-altitude near source + local source | - |
| D | 1.66 μm Weathering and pedogenesis | 5.01 μm Upper westerly transport | 11.48 μm Dry dust | 45.70 μm Low-altitude near source + local source | 831.76 μm Rock weathering |

*5.2. Evolutionary History of Winter Monsoon Based on Grain-Size End Members*

The evolutionary history of the winter monsoon in the northern permafrost region of the Greater Khingan Range since 28.64 ka BP was reconstructed using the winter monsoon components (BEM3 + BEM4 and CEM4) of the BJC-2 (B) and BJC-3 (C) cores (Figure 12).

The following stages were observed:

First stage: This stage lasted from the late Marine Isotope Stage 3 (MIS 3) to the beginning of the LGM (28.64 ka BP to 26.50 ka BP). The winter monsoon component was low in the MIS3a stage, indicating a weak winter monsoon. The climate in the late MIS 3 stage was warm and moist, the soil was well developed, and the vegetation cover was high due to changes in the Earth's orbit [70].

Second stage: This stage occurred during MIS 2, the LGM (26.50–19.00 ka BP). The winter monsoon and the Siberian cold high-pressure air mass were strong, and the climate was cold and dry. Sandstorms were frequent, and permafrost was widespread globally. The winter wind component and the sandy soil reached their peak, indicating that the winter monsoon had strengthened. The aeolian dust flux increased in the North Pacific, the content of coarse particles increased, and permafrost development occurred, showing a good correspondence with the H2 event (25.23 ka BP).

Third stage: This stage represents the last deglaciation (19.00–11.60 ka BP). The winter wind EM components BEM3 + BEM4, CEM4, and the lower values of the components correspond to the weakening of winter winds and temperature increases, corresponding to the Bolling-Allerod (B/A) warm period and the Younger Dryas (YD) event. The YD event of BJC-2 occurred at 12.58–11.66 ka BP, and the YD event of BJC-3 occurred at 12.05–11.04 ka BP. These results correspond well with the winter wind EM component of loess from southern Kazakhstan [71], the Greenland ice core $\delta^{18}$O data [72], and the deep-sea oxygen isotope $\delta^{18}$O data [73]. The H1 cooling event (17.26 ka BP) was also recorded by the winter monsoon component.

Fourth stage: The Holocene major warm period began during the Holocene MIS 1 (11.04–0.27 ka BP). Dong et al. reconstructed the annual average temperature and four-season temperatures of the Loess Plateau over the past 20,000 years by collecting terrestrial mollusks from northern China that accurately reflect climate signals [74]. A warm period occurred from 8 ka BP to 4 ka BP, followed by a cooling trend. This period coincided with an increase in the winter monsoon EM values after 4 ka BP, changes in the winter monsoon components over southern Kazakhstan, a dust flux over the North Pacific, and the East Asian winter monsoon trend (Figure 12). The influence of the soil composition and properties on permafrost development is the most significant near the southern and lower boundary of the permafrost region. The lithology and water content are critical for the maintenance of permafrost islands. Fine-grained soil has a high water-holding capacity and high capillary forces. These conditions are conducive to the development and maintenance of permafrost areas, as a result, frost-heaving and freeze-thaw cycles occur; but the opposite applies to coarse-grained soil [11]. Permafrost areas in the northeast region have degraded due to global warming and frequent human activities, and permafrost islands are disappearing [75]. An increase in coarse sediment sources will exacerbate permafrost degradation.

In summary, the grain-size EMs in the northern permafrost region of the Greater Khingan Range recorded the evolution of the winter monsoon since MIS 3, showing a weak-strong-weak-strong trend. Two anomalous winter monsoon events (H1 and H2), the B/A warm period, the YD events, and global events were recorded. The results demonstrate the global nature of climate change and the interconnectedness of its driving mechanisms. The winter wind was weak in MIS 3a. Then, entering the LGM period, the global climate cooled, the winter monsoon strengthened, the winter wind-source component supply was sufficient, and the permafrost developed rapidly. With the onset of the deglaciation period, the winter monsoon weakened, and the climate warmed during the Holocene major warming period. After the winter monsoon had weakened until about 4 ka BP, it showed a strengthening trend. Under the background of modern global warming, entering more winter wind components will further exacerbate the degradation of permafrost. Therefore, the protection of permafrost in the Greater Khingan Mountains needs to be addressed.
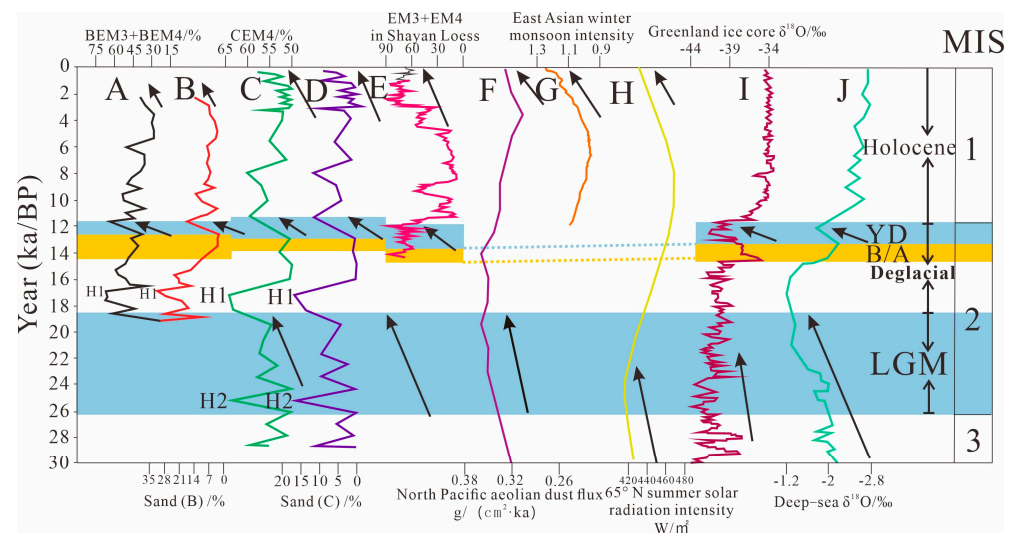
**Figure 12.** (A) BEM3 + BEM4 end-member components; (B) sand content of BJC-2; (C) CEM4 end-member component; (D) sand content of BJC-3; (E) EM3 + EM4 in Shayan Loess, southern Kazakhstan [71]; (F) North Pacific aeolian dust flux [76]; (G) changes in East Asian winter monsoon in the Holocene as indicated by loess Plateau data [77]; (H) 65° N summer solar radiation intensity [78]; (I) Greenland ice core δ18O [72]; and (J) deep-sea oxygen isotopes [73].

## 6. Conclusions

The soil cores obtained from Beiji Town and Huzhong District, Mohe County, were decomposed into four EMs using the EMA method, and core D was decomposed into five EMs. The ultrafine particle component EM1 was derived from weathering and pedogenesis; CEM2 and DEM2 reflected components transported by the upper westerly wind; AEM2, BEM2, and CEM3 represented changes in precipitation. In contrast, DEM3, which exhibited the opposite trend, represents the deposition of dry dust, reflecting the degree of dryness in this region. Together, both reflect the deposition process of dry and wet dust in the region. The dust transport by winter winds included low-level near-source and local-source components, the main sources of soil materials in the permafrost area of the Greater Khingan Range. However, due to the limitations of the EM model, the different cores had one or two EM components, and the local source was likely the soil from the Heilongjiang floodplain; DEM5 was the only large-particle-size component and might represent coarse-grained detritus generated by rock weathering. It was only present in the shallow layer.

The dating data of cores B and C and the winter monsoon components indicated that the winter monsoon in the northern permafrost area of the Greater Hinggan Range exhibited a weak-strong-weak-strong trend since 28.64 ka BP. The winter monsoon components exhibited good correspondence with the Greenland ice core and deep-sea oxygen isotope data, and the winter monsoon was strong in the LGM. During the LGM, winter winds were strong, which provided good conditions for the development of permafrost. Under the trend of global warming, the strengthening of winter winds will cause the transport of coarser particulate matter and further exacerbate permafrost degradation.

**Author Contributions:** Conceptualization, L.L.; methodology, S.Z., X.W. and L.L.; software, L.L. and R.L.; formal analysis, L.L.; investigation, L.L., T.L., J.Z., S.W. and Z.Z.; resources, S.Z.; data curation, L.L.; writing—original draft preparation, L.L.; writing—review and editing, X.W., R.L., L.S. and X.D.; visualization, L.L.; project administration, S.Z.; funding acquisition, S.Z. All authors have read and agreed to the published version of the manuscript.

**Funding:** This research was funded by the Key Joint Program of National Natural Science Foundation of China (NSFC) and Heilongjiang Province for Regional Development (No. U20A2082); National Natural Science Foundation of China (NSFC) (No. 41971151); Natural Science Foundation of Heilongjiang Province of China (No. TD2019D002).

**Data Availability Statement:** Not applicable.

**Conflicts of Interest:** The authors declare that there are no conflict of interest.

## References

1. French, H.M. *The Periglacial Environment*, 3rd ed.; Chichester Wiley: New York, NY, USA, 2007; p. 458.
2. Zhou, Y.; Guo, D.; Qiu, G.; Cheng, G.; Li, S. *Geocryology in China*, 3rd ed.; Science Press: Beijing, China, 2000; pp. 171–194.
3. Jin, H.; Jin, X.; He, R.; Luo, D.; Chang, X.; Wang, S.; Marchenko, S.S.; Yang, S.; Yi, C.; Li, S.; et al. Evolution of permafrost in China during the last 20 ka. *Sci. China Earth Sci.* **2019**, *49*, 1197–1212. [CrossRef]
4. Hou, Y.; Liu, M.; Zhao, C.; Wang, T. A study on the consistency and local characteristics of temperature evolution in Northeast China. *J. Meteor. Environ.* **2019**, *35*, 69–76. (In Chinese)
5. Slater, A.; Lawrence, D. Diagnosing present and Future Permafrost from Climate Models. *J. Clim.* **2012**, *26*, 5608–5623. [CrossRef]
6. Koven, C.; Riley, W.J.; Stern, A. Analysis of permafrost thermal dynamics and response to climate change in the CMIP5 Earth System Models. *J. Clim.* **2013**, *26*, 1877–1900. [CrossRef]
7. Lu, G.; Weng, B.; Guo, D. The geographical boundary of permafrost in the Northeast of China. *J. Glaciol. Geocryol.* **1993**, *15*, 214–218. [CrossRef]
8. Dang, X.; Yu, Y.; Gao, Y.; Yuan, L.; Ma, Y.; Gao, J.; Wang, S.; Zhang, X. Analysis on impact of PLA barrier on soil particle sizes of sand dune. *Res. Soil Water Conserv.* **2014**, *21*, 16–19+24. [CrossRef]
9. Dong, Z.; Li, Z. Wind erodibility of aeolian sand as influenced by grain-size parameters. *J. Soil Water Conserv.* **1998**, *4*, 2–6+13. [CrossRef]
10. Zhao, Y.; Zhao, Q. Reasons of degeneration and tendency of variation of everfrost of the Yellow River source. *Yellow River* **2009**, *31*, 10–12+124. [CrossRef]

11. You, D.; Li, H.; Ge, M.; Zang, S. The influence factors of permafrost active layer depth and their annual change in Heilongjiang Province. *J. Glaciol. Geocryol.* **2018**, *40*, 480–491.

12. Zhou, G.; Huang, X.; Wang, Z.; Zhang, J.; Xie, H. Eolian activity history reconstructed by Bosten Lake grain size data over the past 2000 Years. *J. Desert. Res.* **2019**, *39*, 86–95.

13. Wang, K.; Zheng, H.; Maarten, P.; Zheng, Y. High-Resolution paleoenvironmental record of the mud sediments of the east China sea inner shelf. *Mar. Geol. Quat. Geol.* **2008**, *28*, 1–10.

14. Liu, J.; Wang, H.; Wang, F.; Qiu, J.; Saito, Y.; Lu, J.; Zhou, L.; Xu, G.; Du, X.; Chen, Q. Sedimentary evolution during the last~ 1.9 Ma near the western margin of the modern Bohai Sea. *Palaeogeogr. Palaeoclimatol. Palaeoecol.* **2016**, *451*, 84–96. [CrossRef]

15. Li, Y. *Vertcle Dirtribution and Significance of Polycyclic Aromatic Hydrocarbons and Particle Size in Permafrost of Da Hinggan Mountains*; Harbin Normal University: Harbin, China, 2020.

16. Weltje, G.J. End-member modeling of compositional data: Numerical-statistical algorithms for solving the explicit mixing problem. *Math. Geol.* **1997**, *29*, 503–549. [CrossRef]

17. Qin, X.; Cai, B.; Liu, T. Loess record of the aerodynamic environment in the east Asia monsoon area since 60,000 years before present. *J. Geophys. Res.* **2005**, *110*, B01204. [CrossRef]

18. Yin, Z.; Qin, X.; Wu, J.; Ning, B. The multimodal grain-size distribution characteristics of loess, desert, lake and river sediments in some areas of northern China. *Acta Sedimentol. Sin.* **2009**, *27*, 343–351.

19. Sun, D. Supper-Fine grain size components in Chinese Loess and their palaeoclimatic implication. *Quat. Sci.* **2006**, *26*, 928–936. [CrossRef]

20. Sun, D. Bimode Grain-size distribution of Chinese Loess and its Paleoclimate implication. *Acta Sedimentol.* **2000**, *18*, 327–335. [CrossRef]

21. Yu, X.; Li, H.; Yang, X.; Liu, Z.; Zhang, D.; Ren, X. Grain size characteristics of sediments in the Hunshandake Sandy Land and its implications. *Acta Geogr. Sin.* **2023**, *78*, 1809–1824. [CrossRef]

22. Paterson, G.A.; Heslop, D. New methods for unmixing sediment grain size data. *Geochem. Geophys. Geosyst.* **2015**, *16*, 4494–4506. [CrossRef]

23. Liu, M.; Li, X.; Han, Z.; Chen, Y.; Wang, Y.; Yuan, X.; Ren, Y. Parametric end-member analysis of the grain size distribution of the Xiashu loess and its provenance tracing. *J. Earth Environ.* **2021**, *12*, 510–525. [CrossRef]

24. Wang, T.; Zou, C.; Mao, L.; Zhou, Y.; Mo, D. Sediment grain sieze end-member analysis and its response to climate and sea-level changes in CZ01 borehole on west coast of Bohai Bay. *J. Palaeogeography (Chin. Ed.)* **2022**, *24*, 1224–1237. [CrossRef]

25. Sun, D.; Su, R.; Li, Z.; Lu, H. The ultrafine component in Chinese loess and its variation over the past 7.6 Ma: Implications for the history of pedogenesis. *Sedimentology* **2011**, *58*, 916–935. [CrossRef]

26. Zhao, Q.; Zheng, X.; Zhou, L.; Wang, H.; Lv, H.; Chen, Y.; Ren, S. Grain size end member characteristics and paleoclimatic significance of Loess deposit in Shengshan Island during the Last Glacial Period. *Acta Sedimentol. Sin.* **2022**, 1–18. [CrossRef]

27. Chen, H.; Kong, F.; Xu, S.; Miao, X. Dust accumulation process indicated by grain size end-members of the coastal loess since the Late Pleistocene in Miaodao Islands of Shandong Province. *Quat. Sci.* **2021**, *41*, 1306–1316. [CrossRef]

28. Fang, Y.; Wang, Z.; Wang, Y.; Wang, W.; Fu, C.; Wear, C.; Hu, H.; Kong, X. Grain size end-member components and sedimentary mechanism of Eocene lacustrine sediments in Huangyang River section of Wuwei Basin. *J. Earth Environ.* **2022**, *13*, 296–307. [CrossRef]

29. Yu, T.; Li, X.; Yu, R.; Li, Z.; Sun, Y.; Jiang, Z. Zircon U—Pb ages and geochemistry of monzonite from Xiaokelehe Mo-Cu Deposit in the north of Greater Khingan Mountains. *Gold* **2021**, *42*, 11–19.

30. Hu, H.; Wei, S.; Sun, L. Estimation of carbon emissions due to forest fire in Daxing'an Mountains from 1965 to 2010. *Chin. J. Plant Ecol.* **2012**, *36*, 629–644. [CrossRef]

31. Chang, X.; Jin, H.; He, R.; Jing, H.; Li, G.; Wang, Y.; Luo, D.; Yu, S.; Sun, H. Review of Permafrost Monitoring in the Northern Da Hinggan Mountains, Northeast China. *J. Glaciol. Geocryol.* **2013**, *35*, 93–100.

32. Zhang, J.; Wang, W.; Du, H.; Zhong, Z.; Xiao, L.; Zhou, W.; Zhang, B.; Wang, H. The response of vegetation to the change of active layer thickness in permafrost region of the north Greater Khingan Mountains. *Acta. Ecol. Sin.* **2018**, *38*, 4684–4693.

33. Lv, J.; Li, X.; Hu, Y.; Wang, X.; Liu, H.; Bing, L. Factors affecting the thickness of permafrost's active layer in Huzhong National Nature Reserv. *Chin. J. Ecol.* **2007**, *26*, 1369–1374. [CrossRef]

34. Ran, Y.; Li, X.; Cheng, G.; Che, J.; Aalto, J.; Karjalainen, O.; Hjort, J.; Luoto, M.; Jin, H.; Obu, J.; et al. New high-resolution estimates of the permafrost thermal state and hydrothermal conditions over the Northern Hemisphere. *Earth. Syst. Sci Data.* **2022**, *14*, 865–884. [CrossRef]

35. Reimer, P.J.; Bard, E.; Bayliss, A.; Beck, J.W.; Blackwell, P.G.; Ramsey, C.B.; Buck, C.E.; Cheng, H.; Edwards, R.L.; Friedrich, M. IntCal13 and Marine13 radiocarbon age calibration curves 0–50,000 years cal BP. *Radiocarbon* **2013**, *55*, 1869–1887. [CrossRef]

36. Stueiver, M.; Reimer, P.J. Extended ^{14}C database and revised CALIB radiocarbon calibration program. *Radiocarbon* **1993**, *35*, 215–230. [CrossRef]

37. Blaauw, M.; Christen, J.A. Flexible paleoclimate age-depth models using an autoregressive gamma process. *Bayesian. Anal.* **2011**, *6*, 457–474. [CrossRef]

38. Mcmanus, J. *Techniques in Sedimentology*, 1st ed.; Black-Well: Oxford, UK, 1988; pp. 63–85.

39. Jia, J.; Gao, S.; Xue, Y. Grain size parameters derived from graphic and moment methods: A comparative study. *Oceanol. Limnol. Sin.* **2002**, *33*, 577–582.

40. Wang, Z.; Yu, D.; Luo, F.; Yang, H. Comparison of grain size parameters from graphical and moment methods for surface sediments in Quanzhou Bay. *Mar Geol. Front.* **2016**, *32*, 19–27. [CrossRef]
41. Liu, Y.; Liu, X.; Sun, Y. QGrain: An open-source and easy-to-use software for the comprehensive analysis of grain size distributions. *Sediment. Geol.* **2021**, *423*, 105–980. [CrossRef]
42. Peng, J.; Zhao, H.; Dong, Z.; Zhang, Z.; Yang, H.; Wang, X. Numerical methodologies and tools for efficient and flexible unmixing of single-sample grain-size distributions: Application to late Quaternary aeolian sediments from the desert-loess transition zone of the Tengger Desert. *Sediment. Geol.* **2022**, *438*, 106–211. [CrossRef]
43. Boulay, S.; Colin, C.; Trentesaux, A.; Pluquet, F.; Bertaux, J.; Blamart, D.; Buehring, C.; Wang, P. Mineralogy and Sedimentology of Pleistocene Sediment in the South China Sea (ODP Site 1144). *Proc. Ocean. Drill. Program Sci. Results* **2003**, *184*, 1–21. [CrossRef]
44. Wen, X.; Tonya; Huang, C.; Gombo, S. Multi-material Source of Loess Deposits from the Jiuzhaigou National Nature Reserve on the Eastern Margin of the Tibetan Plateau. *Mountain Research* **2014**, *32*, 603–614. [CrossRef]
45. Cao, B. *Geomorphology and Quaternary Geology*; Geomorphology and Quaternary Geology China University of Geosciences Press: Hubei, China, 1995; pp. 1–288.
46. Shi, Y. Evolution of the Cryosphere in the Tibetan Plateau,China,and its Relationship with the Global Change in the Mid Quaternary. *J. Glaciol. Geocryol.* **1998**, *20*, 197–208. [CrossRef]
47. Pye, K. *Aeolian Dust and Dust Deposits*; Academic Press: London, UK, 1987; pp. 1–256. [CrossRef]
48. Bronger, A.; Heinkele, T. Mineralogical and clay mineralogical aspects of loess research. *Quatern. Int.* **1990**, *7*, 37–51. [CrossRef]
49. Wang, C.; Ye, W.; Yang, L. The content of Fe, Mn, Al, Sr in red and white part of vermicular red clay in Xuancheng profile. *J. Anhui Norm. Univ. (Nat. Sci.)* **2017**, *40*, 271–274. [CrossRef]
50. Sun, D.; Su, R.; Bloemendal, J.; Lu, H. Grain-size and accumulation rate records from Late Cenozoic aeolian sequences in northern China: Implications for variations in the East Asian winter monsoon and westerly atmospheric circulation. *Palaeogeogr. Palaeoclimatol. Palaeoecol.* **2008**, *264*, 39–53. [CrossRef]
51. Meng, Y.; Cao, D.; Wu, Y.; Wang, Z. Comparisons of dynamic dow nscaling of the wind field in forest areas of Da-xiao-Xing'anling Mountains. *J. Meteor. Environ.* **2019**, *35*, 8–15. [CrossRef]
52. Nottebaum, V.; Stauch, G.; Hartmann, K.; Zhang, J.; Lehmkuhl, F. Unmixed loess grain size populations along the northern Qilian Shan (China): Relationships between geomorphologic, sedimentologic and climatic controls. *Quatern. Int.* **2015**, *372*, 151–166. [CrossRef]
53. Sun, D.; Bloemendal, J.; Rea, D.K.; An, Z.; Vandenberghe, J.; Lu, H.; Su, R.; Liu, T. Bimodal grain-size distribution of Chinese loess, and its palaeoclimatic implications. *Catena* **2004**, *55*, 325–340. [CrossRef]
54. Xie, Y.; Chi, Y.; Meng, J.; Guo, L.; Wang, Y. Grain-size and Sr–Nd isotopic compositions of dry-and wet-deposited dusts during the same dust-storm event in Harbin, China: Implications for source, transport–deposition modes, dynamic mechanism and formation of eolian loess. *Environ. Earth Sci.* **2015**, *74*, 6489–6502. [CrossRef]
55. Sun, D.; Bloemendal, J.; Rea, D.; Vandenberghe, J.; Jiang, F.; An, Z.; Su, R. Grain-size distribution function of polymodal sediments in hydraulic and aeolian environments, and numerical partitioning of the sedimentary components. *Sediment. Geol.* **2002**, *152*, 263–277. [CrossRef]
56. Li, X.; Han, Z.; Chen, Y.; Cai, Y.; Yang, D. Characteristics and source of rain dust in Nanjing on 11 March 2006 Quaternary Sciences. *Quat. Sci.* **2009**, *29*, 43–54. [CrossRef]
57. Sun, M.; Yang, S.; Xiao, J.; Wang, Y.; Huang, X.; Zhang, S.; Yang, X.; Jiang, W.; Ding, Z. BrGDGTs-based temperature and hydrological reconstruction from fluvio-lacustrine sediments in the monsoonal North China Plain since 31 kyr BP Quaternary Science Reviews. *Quat. Sci. Rev.* **2022**, *277*, 107268. [CrossRef]
58. Sahu, B.K. Depositional mechanisms from the size analysis of clastic sediments. *J. Sediment. Res.* **1964**, *34*, 73–83. [CrossRef]
59. Pye, K.; Zhou, L.P. Late Pleistocene and Holocene aeolian dust deposition in north China and the northwest Pacific Ocean. *Palaeogeogr. Palaeoclimatol. Palaeoecol.* **1989**, *73*, 11–23. [CrossRef]
60. Tsoar, H.; Pye, K. Dust transport and the question of desert loess formation. *Sdimentology* **1987**, *34*, 139–153. [CrossRef]
61. Wang, S.; Wei, D.; Zhang, W. The End-member characteristics of the grain size of the aeolian sand deposits in the Liaodong Peninsula since the last glacial period and the study on paleoclimate evolution. *Quat. Sci.* **2022**, *42*, 338–349. [CrossRef]
62. Prins, M.A.; Vriend, M. Glacial and interglacial eolian dust dispersal patterns across the Chinese Loess Plateau inferred from decomposed loess grain-size records. *Geochem. Geophys. Geosyst.* **2007**, *8*, 1–17. [CrossRef]
63. Zhang, Y.; Mao, C.; Zhang, J.; Huang, X.; Otgonbayar, D. Aeolian activities in the NW Mongolia during the Holocene recorded by grain-size-sensitive partiles in the sediments of Lake Tolbo. *J. Lake Sci.* **2023**, *35*, 368–380.
64. Vandenberghe, J. Grain size of fine-grained windblown sediment: A powerful proxy for process identification. *Earth-Sci. Rev.* **2013**, *121*, 18–30. [CrossRef]
65. Li, S. *End-Member Analysis of Loess Grain-Size in the Eastern Tibetan Plateau and Its Environmental Implications*; Lanzhou University: Lanzhou, China, 2018.
66. De Moor, J.J.W.; Kasse, C.; Van Balen, R.; Vandenberghe, J.; Wallinga, J. Human and climate impact on catchment development during the Holocene-Geul River, the Netherlands. *Geomorphology* **2008**, *98*, 316–339. [CrossRef]
67. Vandenberghe, J.; Renssen, H.; van Huissteden, K.; Nugteren, G.; Konert, M.; Lu, H.; Andrey, D.; Buylaert, J.P. Penetration of Atlantic westerly winds into Central and East Asia. *Quat. Sci. Rev.* **2006**, *25*, 2380–2389. [CrossRef]

68. Zhang, Q.; Li, Z.; Su, X.; Hu, J. Study on residual soil characteristics of Cote D 'Ivoire, Africa. *Des. Hydroelectr. Power Stn.* **2021**, *37*, 8–12. [CrossRef]

69. Gaudin, A. An investigation of crushing phenomena. *Trans. Am. Inst. Min. Metall. Pet. Eng.* **1926**, *73*, 253–316.

70. Tian, Q.; Yin, J.; Hao, X. MIS3 climate change assessed according to loess deposition in the Linfen Basin, China. *Arid Zone Res.* **2022**, *39*, 10–20. [CrossRef]

71. Su, C.; Xu, Z.; Zhang, D.; Liu, Q.; Liu, J. Aeolian dust history since 14. 4 cal ka BP indicated by grain-size end members of Shayan loess in the southern Kazakhstan. *Quat. Sci.* **2023**, *43*, 46–56. [CrossRef]

72. Dansgaard, W.; Johnsen, S.J.; Clausen, H.B.; Dahl-Jensen, D.; Gundestrup, N.S.; Hammer, C.U.; Hvidberg, C.S.; Steffensen, J.P.; Sveinbjörnsdottir, A.; Jouzel, J. Evidence for general instability of past climate from a 250-kyr ice-core record. *Nature* **1993**, *364*, 218–220. [CrossRef]

73. Linsley, B.K. Oxygen-isotope record of sea level and climate variations in the Sulu Sea over the past 150,000 years. *Nature* **1996**, *380*, 234–237. [CrossRef]

74. Dong, Y.; Wu, N.; Li, F.; Zhang, D.; Zhang, Y.; Shen, C.; Lu, H. The Holocene temperature conundrum answered by mollusk records from East Asia. *Nat. Commun.* **2022**, *13*, 51–53. [CrossRef]

75. Chen, S.; Zang, S.; Sun, L. Characteristics of permafrost degradation in Northeast China and its ecological effects: A review. *Sci. Cold Arid. Reg.* **2020**, *12*, 1–11.

76. Hovan, S.; Rea, D.K.; Pisias, N.G. Late Pleistocene continental climate and oceanic variability recorded in northwest Pacific sediments. *Paleoceanography* **1991**, *6*, 349–370. [CrossRef]

77. Kang, S.; Du, J.; Wang, N.; Dong, J.; Wang, D.; Wang, X.; Qiang, X.; Song, Y. Early Holocene weakening and mid-to late Holocene strengthening of the East Asian winter monsoon. *Geology* **2020**, *48*, 1043–1047. [CrossRef]

78. Berger, A.; Loutre, M.-F. Insolation values for the climate of the last 10 million years. *Quat. Sci. Rev.* **1991**, *10*, 297–317. [CrossRef]